Proximity-induced superconductivity in Weyl semimetals

Udit Khanna,[1] Arijit Kundu,[2] Saurabh Pradhan,[1] and Sumathi Rao[1,3]
[1]*Harish-Chandra Research Institute, Chhatnag Road, Jhunsi, Allahabad 211 019, India*
[2]*Department of Physics, Indiana University, 727 East Third Street, Bloomington, Indiana 47405-7105, USA*
[3]*International Center for Theoretical Studies, Tata Institute of Fundamental Research, IISc Campus, Bangalore 560012, India*
(Received 31 July 2014; revised manuscript received 3 November 2014; published 20 November 2014)

We study superconducting proximity effects in Weyl semimetals (WSM) with broken time-reversal symmetry by tunnel-coupling one of its surfaces to an s-wave superconductor using the Green's function approach. We find that the band structure develops coherence peaks, but despite the presence of metallic states in the bulk, the coherence peaks do not extend far into the bulk and remain confined to a few layers close to the interface, similar to the proximity effect in the topological insulators (TI) which are gapped in the bulk. The Weyl nodes remain unaffected, and in that sense, no true gap develops. We also study the induced p- and s-wave pairing amplitudes classified by their symmetries, as a function of the various parameters of the theory, and note the exponential decay of the induced pairings in the bulk both in the TI and the WSM, even at finite chemical potential.

DOI: 10.1103/PhysRevB.90.195430 PACS number(s): 74.45.+c, 73.20.At, 74.78.Na

I. INTRODUCTION

In recent years, topology has become an important tool in classifying the phases of matter [1]. Although the study of topological phases started with the discovery of the quantum Hall and fractional quantum Hall phases [2] in the 1980s, it gained momentum with the discovery of the time-reversal-invariant topological insulators [3] a few years ago. Topological insulators (TI) are classified in terms of their bulk band structure, and by now there has been a complete classification of free-fermion topological insulators in the presence of disorder [4,5]. All these phases have topologically nontrivial momentum-space structure, are insulating in the bulk, and have metallic surface states.

It has been generally assumed that it is the gap in the bulk electronic spectrum which makes the topologically nontrivial ground state with its surface states stable and unable to decay to the topologically trivial phase. However, more recently it has been shown that it is possible to have nontrivial momentum-space topology even for gapless fermionic systems. One such recently identified system is the Weyl semimetal phase [6,7] which has isolated gapless points (Weyl nodes) in the bulk spectrum, where exactly 2 bands touch. The low-energy behavior close to these points is given by a Weyl Hamiltonian of fixed chirality. The Weyl nodes are topologically protected, because a gap cannot be opened unless two nodes of opposite chirality are coupled. The band structure shows unusual surface states called Fermi arcs [6], which has led to many interesting work [8]. The topological response of the phase has been argued to be a realization of the Adler-Bell-Jackiw anomaly [9] in condensed matter systems. There are several recent reviews [10] which have discussed various interesting properties of Weyl semimetals.

The introduction of superconductivity in topological insulators characterizes a new exotic phase, the topological superconductor, whose inherent particle-hole symmetry leads to surface states that support Majorana fermions. The superconductor-doped TI $Cu_xBi_2Se_3$ [11] was theoretically predicted [12,13] to be a TI and experimental evidence was obtained [14] using point-contact spectroscopy to detect the itinerant massless Majorana state on the surface. The introduction of superconductivity via the proximity effect [15] has also led to considerable work on topological insulator–superconductor hybrid junctions [16–19] with special attention to the surface states that develop between them. Proximity with an s-wave superconductor was shown to lead to a significant renormalization of the parameters in the effective model for surface states. It was also shown that when the Fermi surface is close to the surface Dirac cone vertex, the electrons exhibit s-wave pairing, but away from the vertex, the triplet component increases in amplitude. A full symmetry classification of all the induced pairings for proximity to s-wave, p-wave, and d-wave superconductors was also studied [20,21] and it was shown that the different induced pairing amplitudes modify the density of states at the interface significantly [22,23].

Similarly, one might expect that the introduction of superconductivity in the Weyl semimetal (WSM) would also lead to new phenomena. A heterostructure of topological insulators and s-wave superconductors was studied by Meng and Balents [24] who showed that superconductivity split the Weyl modes into Bogoliubov-Weyl modes. By studying vortices in some of these phases, characterized by different number of Weyl modes, they found zero-energy Majorana modes under some conditions. Cho *et al.* [25] studied superconducting states of doped inversion symmetric Weyl semimetals and showed that the finite-momentum FFLO pairing state is energetically favored over the even-parity BCS state. Recently, Lee *et al.* [26] studied the proximity effect in topological insulators, when the chemical potential is close to but not in the bulk gap. They found that the superconducting gap penetrates the bulk and is observable at the naked surface, opposite to the one in proximity to the superconductor.

However, there has been no systematic study of proximity-induced superconductivity in Weyl semimetals, which is the main focus of this paper. Since our model also includes the topological insulator phase for some region of parameter space, we also provide results for proximity-induced superconductivity for topological insulators in our model for comparison. Our model consists of a 3D topological insulator, converted to a Weyl semimetal, by including either parity-breaking terms or time-reversal breaking terms, or both. Time-reversal breaking leads to Weyl nodes at the same energy and surface states, which form a Fermi arc between the nodes, whereas parity

breaking leads to Weyl nodes at different energies and no Fermi arcs. The dispersion of the Fermi arcs or surface states is flat in a particular direction and chiral in the other direction and points along the Fermi arc can be understood as the edge states of a two-dimensional Chern insulator. When inversion symmetry is broken, however, the Weyl nodes are separated in energy and we do not get surface states, distinct from the bulk. Since we are mainly interested in the new physics coming from the Fermi arc states, unless otherwise specified, in this paper we always consider the Weyl semimetal phase induced by having a time-reversal-breaking perturbation.

Superconductivity is then induced in the semimetal by coupling it to an s-wave superconductor on one of its surfaces. We compute the self-energy of the topological insulator/semimetal electrons by integrating out the superconductor degrees of freedom and use the imaginary part of the Green's function to compute the local density of states (LDOS). We find that the superconductor induces coherence peaks on the LDOS of the electrons on a few layers close to the interface and we contrast the behavior of the LDOS on different layers for the TI and the WSM. For the TI, we find the reduction in the LDOS close to $\omega = 0$ which is the hallmark of the gap formation, whereas for the WSM, we find that the enhancement of the density of states without a superconductor (the hallmark of the flat band) splits into two bands with a reduction of the density of states at $\omega = 0$. We study in detail the band structure of the surface states and find that the surface state of the TI is completely gapped by the proximity effect, whereas the surface states of the WSM get split and acquire a small gap, but the Weyl nodes remain unaffected. Thus the surface band acquires a superconducting gap in a TI, but no true superconducting gap is induced in WSM [24].

We also study the behavior of the induced pairing amplitudes (singlet, triplet, intraorbital, and interorbital) as a function of the various parameters in the theory. As shown in Ref. [20], the induced pairing amplitudes in Bi_2Se_3-type materials with tetragonal symmetry are classified in terms of the irreducible representations Γ of the D_{4h} group. Since we are only considering proximity with an s-wave conductor in this paper, we are only interested in representations with total angular momentum $J_z = 0$. We find that the induced pairings fall off exponentially fast away from the interface both in the TI and in the WSM. But they are not very sensitive to other parameters such as the chemical potential and the time-reversal-breaking parameters. The induced pairings increase as a function of the superconducting pairing amplitude of the superconductor and the coupling of the superconductor to the TI/WSM. It is also perhaps worth mentioning that both in the singlet and triplet amplitudes, the symmetries of the two largest amplitudes reverse between the TI and the WSM, with interorbital pairings being larger in the TI and intraorbital pairings being larger in the WSM.

II. MODEL SYSTEM

We start with a simple tight-binding four-band lattice model for the topological insulator (TI) in three dimensions (3DTI), which can describe strong and weak topological insulators, Weyl semimetals, and ordinary insulators depending on the parameters of the model. The Bi_2Se_3 family of 3DTI have an effective description in terms of the Hamiltonian given by $H_0 = H_C + H_{SO}$ [27] with

$$\begin{aligned} H_C &= \epsilon \sum_{\boldsymbol{r}} \psi^\dagger_{\boldsymbol{r}} \tau_x \psi_{\boldsymbol{r}} - t \sum_{\langle \boldsymbol{r},\boldsymbol{r}'\rangle} \psi^\dagger_{\boldsymbol{r}} \tau_x \psi_{\boldsymbol{r}'} + \text{H.c.}, \\ H_{SO} &= i\lambda_{SO} \sum_{\boldsymbol{r}} \psi^\dagger_{\boldsymbol{r}} \tau_z (\sigma_x \psi_{\boldsymbol{r}+\boldsymbol{y}} - \sigma_y \psi_{\boldsymbol{r}+\boldsymbol{x}}) \\ &\quad + i\lambda_z \sum_{\boldsymbol{r}} \psi^\dagger_{\boldsymbol{r}} \tau_y \psi_{\boldsymbol{r}+z} + \text{H.c.}, \end{aligned} \tag{1}$$

where $\psi_{\boldsymbol{r}}$ is the fermion operator in TI region. $\boldsymbol{r}, \boldsymbol{r}'$ refer to site indices in all three dimensions (in the TI region) and $\boldsymbol{r} + \boldsymbol{x}$ refers to the nearest neighbor of site at $\boldsymbol{r}$ in the x direction (similarly for y and z directions). Here z is taken as the growth direction and $\boldsymbol{\sigma}$ and $\boldsymbol{\tau}$ denote Pauli matrices in spin and parity (orbital) space, respectively. ϵ and t denote the on-site and nearest-neighbor hopping amplitudes. λ_{SO} and λ_z are the (possibly anisotropic) spin-orbit (SO) interaction strengths in the $x - y$ plane and in the z direction, respectively.

The topological invariants for the 3DTI, $\nu_\mu = (\nu_0; \nu_1, \nu_2, \nu_3)$, can be computed easily (due to parity invariance [15]) and are given by

$$\begin{aligned} (-1)^{\nu_0} &= \text{sgn}[(\epsilon - 6t)(\epsilon + 6t)(\epsilon - 2t)^3(\epsilon + 2t)^3], \\ (-1)^{\nu_i} &= \text{sgn}[(\epsilon + 6t)(\epsilon - 2t)(\epsilon + 2t)^2], \end{aligned}$$

for $i = 1,2,3$. This implies that we have the following phases:

$$\begin{aligned} &|\epsilon| > |6t|, \quad \nu_\mu = (0;0,0,0), \quad \text{ordinary insulator;} \\ &|6t| > |\epsilon| > |2t|, \quad \nu_0 = 1, \quad \text{strong TI;} \\ &|2t| > |\epsilon| > 0, \quad \nu_0 = (0;1,1,1), \quad \text{weak TI.} \end{aligned} \tag{2}$$

At the boundaries of the topological phase transitions (at $\epsilon \approx \pm 6t, \pm 2t$), the bulk gap closes and the effective Hamiltonian is a massless Dirac Hamiltonian. By introducing either parity (inversion) or time-reversal (TR) symmetry breaking perturbations to the Hamiltonian H_0, the Dirac node can be split in 2 Weyl nodes separated in energy or momentum, respectively. Thus the Hamiltonian for the WSM is given by $H_W = H_0 + H_E$, where

$$H_E = \sum_{\boldsymbol{r}} \psi^\dagger_{\boldsymbol{r}} (b_0 \tau_y \sigma_z - b_x \tau_x \sigma_x + b_y \tau_x \sigma_y + b_z \sigma_z) \psi_{\boldsymbol{r}}. \tag{3}$$

Here b_0 and $\boldsymbol{b}$ are parameters that break inversion and TR symmetry, respectively [27]. Note that the Dirac node mentioned here is the 3D Dirac node that occurs in the bulk spectrum at the phase transition between the normal and topological insulator and should not be confused with the 2D Dirac nodes, which occur in the surface spectrum of the TI phase. The phase diagram of the different phases in this model is given in Fig. 1.

For finite systems, both TI and WSM phases give rise to surface states. For strong topological insulators, surface states exist on each surface as midgap states [3], whereas in weak topological insulators, surface states arise only on particular surfaces depending on the values of ν_i $(i = 1,2,3)$ [28]. For Weyl semimetals (within this model), if only inversion symmetry is broken, the Weyl nodes are separated in energy and there are no surface states separable from the bulk states. Surface states arise only when TR symmetry is broken. As an

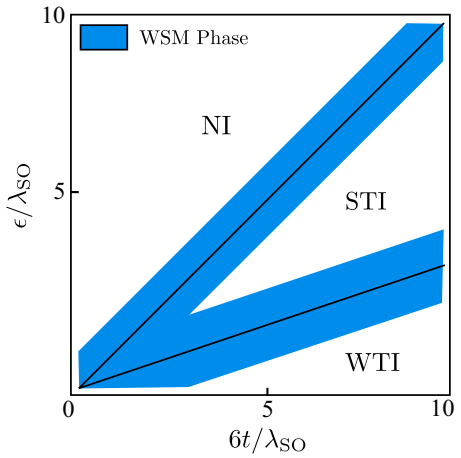

FIG. 1. (Color online) A typical phase diagram of our model system. The Weyl semimetal (WSM) phase appears at the strong topological insulator (STI) / normal insulator (NI) ($\epsilon = 6t$) and strong topological insulator (STI) / weak topological insulator (WTI) ($\epsilon = 2t$) boundaries with broken time reversal / parity perturbations. The WSM phase extends with increasing perturbations (blue filled region). Parameters used here are $\lambda_z = \lambda_{SO}$ and $\boldsymbol{b} = (0.6\lambda_{SO},0,0)$.

example, if the TR symmetry is broken by $\boldsymbol{b} = b_x\hat{x}$, then the Weyl nodes occur with a separation of $b_x/\lambda_z\hat{x}$ in momentum space. In this case, we find that surface states exist on the surfaces parallel to the x-y and x-z planes (not on the third plane). For a large enough system, the dispersion of surface states is flat between the two Weyl nodes along the k_x direction, and is linear along k_y (on the x-y plane) or k_z (on the x-z plane). The surface states exist only between the two Weyl nodes and the states on opposite surfaces have opposite chiralities, as illustrated in Fig. 2. These are the Fermi arc states. Fermi arcs can be understood as the edge states of a Chern insulator that

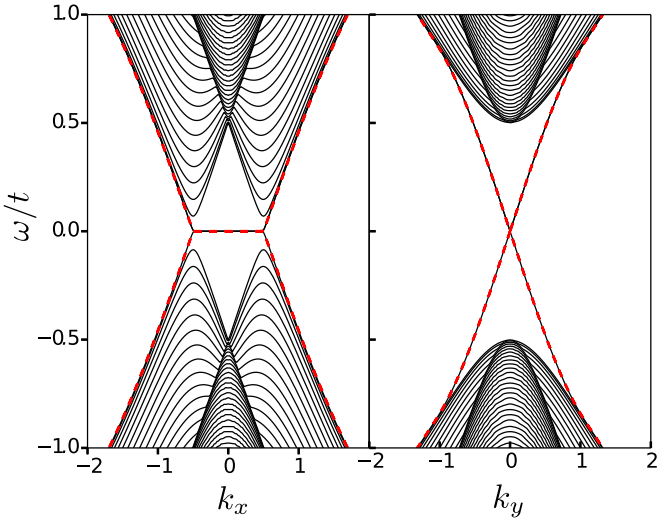

FIG. 2. (Color online) The dispersion for a WSM with 2 Weyl nodes at $\pm b_x/\lambda_z$ is shown along k_x and k_y. The parameters used are $\boldsymbol{b} = (0.50t,0,0)$,$\lambda_{SO} = \lambda_z = 0.50t$. The dashed (red) lines denote both the surface bands. Note that the surface states at opposite ends have opposite chirality.

exists for each value of k_x between the Weyl nodes. It may also be worth noting that the WSM formed near $\epsilon \sim 6t$ and $\epsilon \sim 2t$ have their chiralities reversed for the top and bottom edges.

For the rest of this paper, we concentrate on the TR-broken Weyl semimetal, with $b_0 = 0$ and $\boldsymbol{b} \neq 0$, since we are interested in the proximity effect of the superconductor on the surface, i.e., on the Fermi arc states.

III. COUPLING TO THE SUPERCONDUCTOR

We now couple one of the surfaces of the WSM to an s-wave superconductor as shown in Fig. 3. The bulk Hamiltonian of the s-wave superconductor is given by

$$H_S = \epsilon_{sc}\sum_{\boldsymbol{R},\sigma}\Phi^\dagger_{\boldsymbol{R},\sigma}\Phi_{\boldsymbol{R},\sigma} - t_{sc}\sum_{\langle\boldsymbol{R},\boldsymbol{R}'\rangle,\sigma}\Phi^\dagger_{\boldsymbol{R},\sigma}\Phi_{\boldsymbol{R}',\sigma} + \sum_{\boldsymbol{R}}\Delta\Phi^\dagger_{\boldsymbol{R},\uparrow}\Phi^\dagger_{\boldsymbol{R},\downarrow} + \text{H.c.}, \quad (4)$$

where Φ is the fermion operator in the superconductor. $\boldsymbol{R},\boldsymbol{R}'$ refer to site index in all three directions (in the superconducting region). ϵ_{sc} and t_{sc} denote the on-site energy and nearest-neighbor hopping amplitudes in the superconductor, respectively. The coupling is a tunneling term between the top layer of the superconductor and the bottom layer of the WSM:

$$H_T = \sum_{\boldsymbol{r}_c,\tau,\sigma}\tilde{t}_\tau\psi^\dagger_{\boldsymbol{r}_c,\tau,\sigma}\Phi_{\boldsymbol{r}_c+z,\sigma} + \text{H.c.}, \quad (5)$$

where $\boldsymbol{r}_c$ denotes the sites in the last layer of the WSM (perpendicular to the interface) and $\boldsymbol{r}_c + z$ denotes the first layer of the superconductor. τ denotes the orbital in the WSM and σ is the spin. $\tilde{t}_\tau$ is the tunneling amplitude which can be different for the two orbitals. In this work, we have assumed that t_τ is the same for both orbitals for simplicity. Using different tunneling amplitudes for the two orbitals will change the results quantitatively, but not qualitatively. For detailed results as a function of the ratio of the tunneling amplitudes for the TI, see [20].

The Nambu basis for the fermions in the WSM, denoted by $\tilde{\Psi}^\dagger_{\boldsymbol{r}}$, is given by

$$(\psi^\dagger_{\boldsymbol{r},\uparrow,1},\psi^\dagger_{\boldsymbol{r},\downarrow,1},\psi^\dagger_{\boldsymbol{r},\uparrow,2},\psi^\dagger_{\boldsymbol{r},\downarrow,2},\psi_{\boldsymbol{r},\downarrow,1},-\psi_{\boldsymbol{r},\uparrow,1},\psi_{\boldsymbol{r},\downarrow,2},-\psi_{\boldsymbol{r},\uparrow,2}), \quad (6)$$

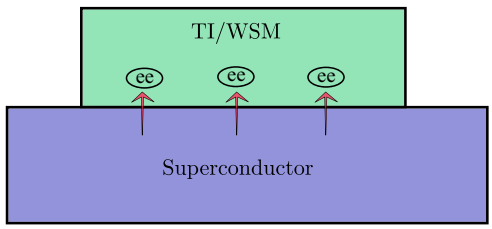

FIG. 3. (Color online) Schematic of our setup. An s-wave superconductor is coupled with the Weyl semimetal/topological insulator system through proximity. Cooper pairs from the superconductor diffuse into the bulk of the Weyl semimetal/topological insulator giving rise to induced superconductivity.

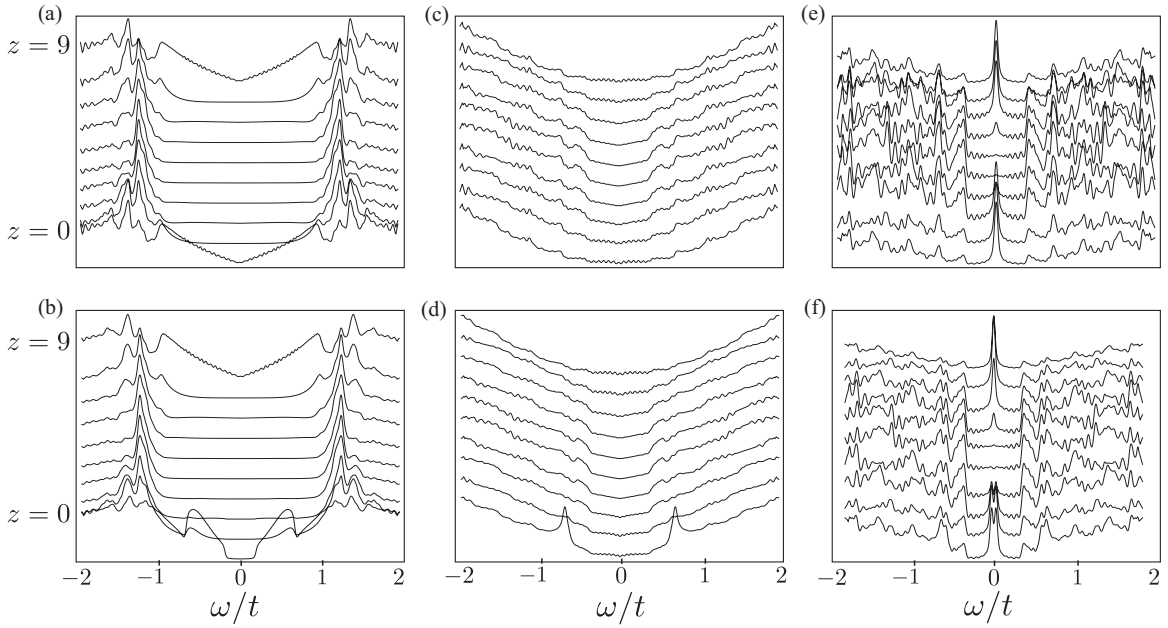

FIG. 4. LDOS for the TI and the WSM, with the top row without coupling to the superconductor and the bottom row with coupling to the superconductor. (a) and (b) show the LDOS for the TI integrated over all momenta without and with coupling to the superconductor, respectively. (c) and (d) show the same for the WSM. (e) and (f) show the LDOS at $k_y = 0$ summed over all k_x for the WSM without and with coupling to the superconductor, respectively. The LDOS for the different layers are vertically offset for visibility. The parameters used are $\lambda_{SO} = \lambda_z = 0.5t$, $\Delta = 0.7t$, $\epsilon = 4t$ (for TI) or $\epsilon = 6t$ (for WSM) and $\boldsymbol{b} = (0.5t,0,0)$ for WSM.

where $\uparrow,\downarrow$ refer to the spin and 1,2 refer to the orbitals. Since the Hamiltonian is quadratic in the superconductor degrees of freedom Φ, we can integrate them out and compute an effective action for the WSM. Following the analysis for the self-energy in Ref. [29], we decouple the superconductor and TI degrees of freedom and define the (Nambu-Gorkov) Green's function $G(\omega)$ for the WSM. The derivation is sketched in the Appendix. The Green's function is

$$G(\omega) = [(\omega + i\delta)\mathbf{I} - H_W - \Sigma(\omega)]^{-1}\,, \tag{7}$$

where the self-energy is

$$\Sigma_{\boldsymbol{r}}(\omega) = \delta_{\boldsymbol{r},\boldsymbol{r}_c}\frac{\pi N(0)(\tilde{t})^2}{\sqrt{\Delta^2 - \omega^2}}[\omega\mathbf{I}_\eta - \Delta\eta^x](\mathbf{I}_\tau + \tau^x)\mathbf{I}_\sigma \tag{8}$$

with $\boldsymbol{r}_c$ denoting the sites in the last layer of WSM. Note that the G at each site is an 8×8 matrix comprising the spin, orbital, and particle-hole pseudospin subspaces. Here, we have used only the local (on-site) component of the self-energy. This approximation usually works very well and we shall justify this in the last section by comparing our results with this approximation to the result obtained using exact diagonalization.

IV. LDOS AND THE PAIRING AMPLITUDE

In this section, we use the Green's function to obtain the local density of states (LDOS) and the induced pairing amplitude both in the TI and WSM phases and discuss the dependence of the pairing on the various parameters of the model.

Using the Green's function that we derived in the previous section, we can compute the local density of states (LDOS) in the TI/WSM using

$$D(\omega,\boldsymbol{r}) = -\frac{1}{\pi}\sum_{\sigma,\tau}\mathrm{Im}G^{\sigma\tau}_{\boldsymbol{r}\boldsymbol{r}}\,, \tag{9}$$

σ and τ being the spin and orbital index. As we increase the coupling to the superconductivity, the LDOS shows the appearance of coherence peaks in the band structure as a signature of proximity-induced superconductivity. This is shown in the panel in Fig. 4 where we have plotted the LDOS at different values of z, the layer index, both for the TI and the WSM. Panels (a) and (b) show the LDOS as a function of energy (summed over all momenta) for the TI. Note the Dirac spectrum feature of the surface states for the TI (layers $z = 0$ and $z = 9$). We can also clearly see the dip in the density of states and the appearance of the coherence peaks in the first 2 layers. The coherence peaks are not sharp because we are at zero doping. (For the TI, the sharpness of the coherence peaks increases with the doping, due to the increase in density of states. For WSM, we have checked that there is no significant change when the doping is increased, because there is a significant density of states at the Weyl node even at zero doping.) Panels (c) through (f) are for the Weyl semimetal, with (c) and (d) being the LDOS summed over all momenta and (e) and (f) being the LDOS at $k_y = 0$ summed over all k_x. First, we note the absence of the Dirac spectrum feature in the edge states. Instead, there is peak in the DOS at $\omega = 0$ (and $k_y = 0$) which is the signature of the flat band in the absence of coupling to the superconductor. (This feature gets lost when all k_y is summed over, which is why we have also chosen to show the band structure without summing over k_y.) With the coupling to the superconductor, the single peak splits

into two with a small gap. The effect of the proximity of the superconductor on the surface states will be studied in greater detail in the next section.

Following [30], we now define the different induced pairing amplitudes. Assuming translation invariance in the x and y directions, we go to momentum space $\boldsymbol{k} = (k_x, k_y)$ in two directions. For each momentum $\boldsymbol{k}$ and each z coordinate, the Green's function can be written as

$$G_{z,\boldsymbol{k}}(\omega) = \begin{pmatrix} h_z(\omega,\boldsymbol{k}) & \bar{\Delta}_z(\omega,\boldsymbol{k}) \\ \bar{\Delta}_z^*(\omega,\boldsymbol{k}) & h_z'(\omega,\boldsymbol{k}) \end{pmatrix}. \tag{10}$$

The 4×4 pairing matrix $\bar{\Delta}_{z;\sigma\tau,\sigma'\tau'}(\omega,\boldsymbol{k})$ is related to the pairing amplitudes as

$$\begin{aligned}\bar{\Delta}_{z;\sigma\tau,\sigma'\tau'}(\omega,\boldsymbol{k}) &= \int_0^\infty \frac{dt}{2\pi} \langle c_{z,-\boldsymbol{k},\sigma,\tau}(t) c_{z,\boldsymbol{k},\sigma',\tau'}(0)\rangle e^{i\omega t} \\ &= \int_0^\infty \frac{dt}{2\pi} \hat{\Delta}_{z;\sigma\sigma'\tau\tau'}(\boldsymbol{k},t) e^{i\omega t},\end{aligned} \tag{11}$$

where the last equality defines $\hat{\Delta}_{z;\sigma\sigma'\tau\tau'}(\boldsymbol{k},t)$. We only consider the equal-time ($t = 0$) pairing amplitudes from here on. It is useful to form combinations of the pairing amplitudes which are even (+) or odd (−) under exchange of orbital index as

$$\begin{aligned}\hat{\Delta}^{i\pm}_{z;\sigma\sigma'}(\boldsymbol{k}) &= \hat{\Delta}_{z;\sigma\sigma',11}(\boldsymbol{k}) \pm \hat{\Delta}_{z;\sigma\sigma',22}(\boldsymbol{k}), \\ \hat{\Delta}^{I\pm}_{z;\sigma'\sigma}(\boldsymbol{k}) &= \hat{\Delta}_{z;\sigma\sigma',12}(\boldsymbol{k}) \pm \hat{\Delta}_{z;\sigma\sigma',21}(\boldsymbol{k}),\end{aligned} \tag{12}$$

where the superscript i or I on the left-hand side refers to intraorbital and interorbital pairings. Each of these $\hat{\Delta}$ is a 2×2 matrix in spin space and can be written as a sum of singlet and triplet components:

$$\hat{\Delta}(\boldsymbol{k}) = i\sigma^y \psi(\boldsymbol{k}) + i\sigma^y (\mathbf{d}(\boldsymbol{k})\cdot\boldsymbol{\sigma}), \tag{13}$$

where due to Fermi statistics, $\psi(\boldsymbol{k})$ is even and $\mathbf{d}(\boldsymbol{k})$ is odd under $\boldsymbol{k}\to -\boldsymbol{k}$ for $i\pm$ and $I+$ pairings, whereas $\psi(\boldsymbol{k})$ is odd and $\mathbf{d}(\boldsymbol{k})$ is even under $\boldsymbol{k}\to -\boldsymbol{k}$ for I pairings. Then, the even and odd intraorbital and even interorbital amplitudes have the usual s-wave spin-singlet and p-wave spin-triplet pairing while the odd interorbital amplitude has a p-wave spin-singlet and s-wave spin-triplet pairing. Reference [20] found that an s-wave superconductor does not induce even frequency–odd interorbital pairings in TI (although a p-wave superconductor can do so); however, it does induce odd frequency–odd interorbital pairings. In this work, since we are only interested in equal-time correlations, we ignore the even frequency–odd interorbital and all odd frequency pairing amplitudes.

The Hamiltonian of the Bi_2Se_3-type material considered here has tetragonal symmetry (since it is written on a cubic lattice) and the induced pairings are classified in terms of the irreducible representations Γ of the D_{4h} group [20]. Thus, $\psi(\boldsymbol{k})$ and $\mathbf{d}(\boldsymbol{k})$ must have a functional dependence on $\boldsymbol{k}$, which forms an irreducible representation of D_{4h}. Since we are only considering proximity with an s-wave superconductor in this paper and assuming that the angular momentum in the $\hat{z}$ direction is conserved in the tunneling process, there are only three relevant representations: A_{1g}, A_{1u}, and A_{2u}. Up to linear order in $\boldsymbol{k}$ (and taking $k_z = 0$) we have $\psi(\boldsymbol{k}) = 1$ for A_{1g}, $\mathbf{d}(\boldsymbol{k}) = (k_x, k_y, 0)$ for A_{1u}, and $\mathbf{d}(\boldsymbol{k}) = (k_y, -k_x, 0)$ for A_{2u}. On a square lattice, we may replace $\boldsymbol{k}^2$ by $1-\cos(\boldsymbol{k})$ and terms linear in $\boldsymbol{k}$ by $\sin(\boldsymbol{k})$. We can then classify the $\hat{\Delta}(\boldsymbol{k})$

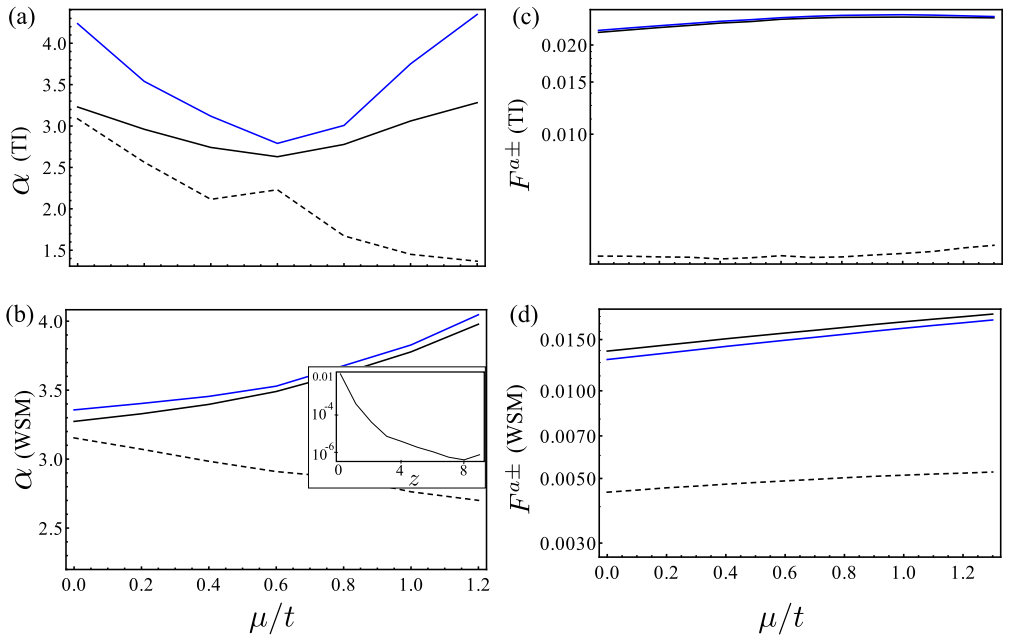

FIG. 5. (Color online) (a) and (b) show the exponential parameter α of the decay (in the unit of 1/lattice spacing in z) for various cases in the TI/WSM, as a function of the chemical potential μ/t. They are denoted by the black and blue (gray) solid lines for s-wave intra- and interorbital amplitudes, respectively, and the black line for p-wave intraorbital amplitude. In the inset of (b), we show a typical exponential decay of the pairing in the bulk. The case shown here is the decay of intraorbital s-wave pairing in the WSM. (c) and (d) show the almost flat behavior of the pairing amplitudes $F^{a\pm}$ as defined in Eq. (15) at $z = 0$ as a function of the chemical potential. The various parameters used are $\lambda_{SO} = \lambda_z = 0.5t$, $\Delta = 0.7t$, $\lambda_S = 0.3t$, $\epsilon = 6t$, $\boldsymbol{b} = (0.5t, 0, 0)$ for WSM and $\epsilon = 4t$, $\boldsymbol{b} = (0,0,0)$ for TI.

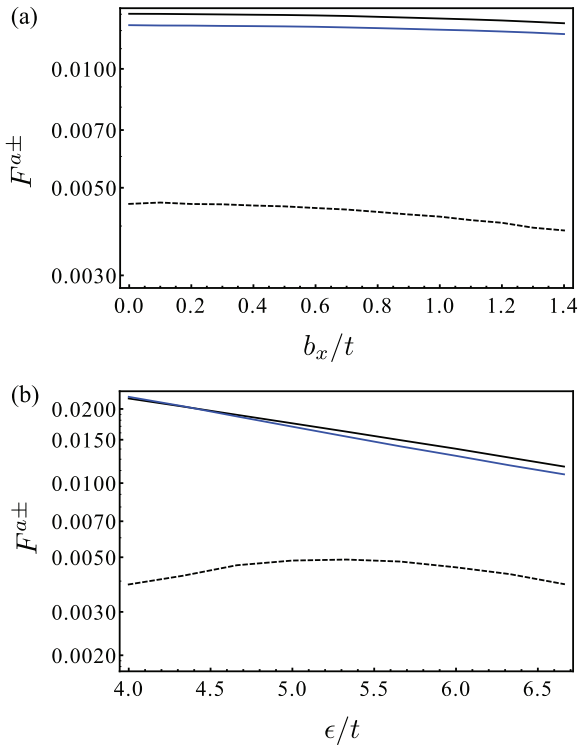

FIG. 6. (Color online) The pairing amplitudes as a function of (a) the time-reversal breaking parameter b_x/t and (b) ϵ/t. The different pairing amplitudes are denoted by the black and blue (gray) solid lines as s-wave intraorbital and interorbital amplitudes, respectively, and the black line as p-wave intraorbital amplitude. Note the crossing of the black and blue lines (crossing of intra- and interorbital pairings) as a function of ϵ/t. Various parameters used are $\lambda_{SO} = \lambda_z = 0.5t$, $\Delta = 0.7t$, $\lambda_S = 0.3t$. For (a), we have used $\epsilon = 6t$, and $\boldsymbol{b} = (0,0,0)$ for (b).

found numerically by finding their inner product with the basis functions. For this, we define

$$F^{a\pm}_{\sigma\sigma'} = \frac{1}{2N_{\boldsymbol{k}}} \sum_{\boldsymbol{k}} S^*_{\sigma\sigma'}(\boldsymbol{k}) \hat{\Delta}^{a\pm}_{\sigma'\sigma}(\boldsymbol{k}), \tag{14}$$

where $S_{\sigma\sigma'}(\boldsymbol{k})$ is one of the basis functions given above. The superscript $a = i, I$ refers to intra- and interorbital pairing, respectively. Then the inner product is

$$F^{a\pm} = \sum_{\sigma\sigma'} F^{a\pm}_{\sigma\sigma'}. \tag{15}$$

We find that the spin-singlet amplitudes have a dominant component with A_{1g} pairing as expected, but the triplet components have A_{2u} pairing and not A_{1u} in both TI and WSM [31]. This is due to the form of the spin-momentum locked low energy Dirac surface state which enforces the vanishing of the A_{1u} triplet amplitude [20].

We note that for the spin singlet, the odd intraorbital pairing is lower by two orders of magnitude compared to the even orbital pairings. Thus, only s-wave spin singlets with even orbital pairings are dominant. For spin triplet, the even orbital pairings are lower by two orders of magnitude with respect to the odd intraorbital pairing. Thus, a p-wave spin triplet with odd intraorbital pairing is dominantly induced. Hence, for both the TI and the WSM, we only display the behavior of the following three amplitudes: spin-singlet even intra- and interorbital pairing and spin-triplet odd intraorbital pairing.

In both the TI and the WSM, the pairing amplitudes fall off exponentially in the bulk [16,26]. The fall-off can be numerically fitted to an exponential $F \propto e^{-\alpha z}$, where the direction z is perpendicular to the surface of contact to the superconductor. In Figs. 5(a) and 5(b) we show how α varies for the various pairing amplitudes as a function of the chemical potential μ for TI and the WSM. We note that α starts to decrease as we increase μ in the case of TI, both for s- and p-wave amplitudes, which means a greater penetration [26]. For the case of WSM, the s-wave pairing has a decreased penetration with increasing μ in contrast to the TI, whereas the p-wave pairing has mildly increasing penetration.

In Figs. 5(c) and 5(d) we compare how the various pairing amplitudes at $z = 0$ for the TI and the WSM change as a function of the chemical potential μ/t. We note that the spin-singlet amplitudes are higher than the spin-triplet amplitudes in all cases. There is also not much variation between the TI and the WSM as far as the spin-singlet amplitudes are concerned. But the spin-triplet amplitudes have substantially larger variation between the TI and the WSM.

We have also studied the behavior of these pairing amplitudes in both the TI and the WSM as a function of various other parameters. The pairing amplitudes remain flat with

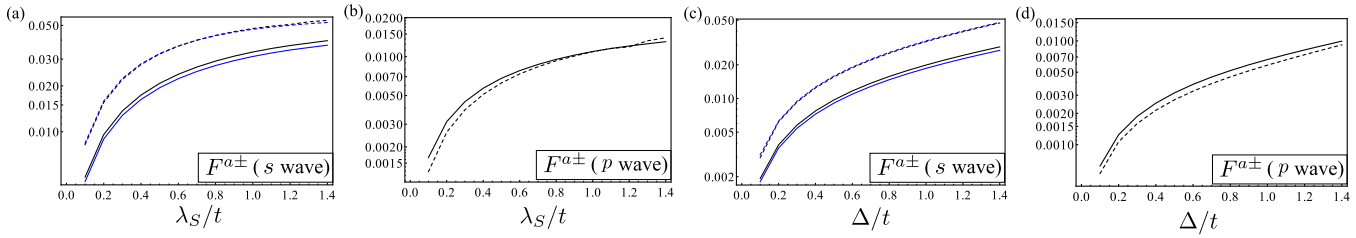

FIG. 7. (Color online) We depict the pairing amplitudes $F^{a\pm}$ as defined in Eq. (15) at $z = 0$ for the intra- and interorbital s-wave and intraorbital p-wave channels as a function of the various parameters in the model. The black and blue (gray) solid lines denote intra- and interorbital pairing for WSM respectively, whereas the black and blue (gray) dashed lines mark intra- and interorbital pairing for TI, respectively. (a) and (b) show the increase in both the s-wave and p-wave pairing channels as a function of the coupling λ_S between the superconductor and the WSM/TI. (c) and (d) show the increase as a function of the superconducting s-wave pairing amplitude Δ in the superconductor. Various parameters used, which are not varied, are $\lambda_{SO} = \lambda_z = 0.5t$, $\Delta = 0.7t$, $\lambda_S = 0.3t$, $\epsilon = 6t$, $\boldsymbol{b} = (0.5t,0,0)$ for WSM and $\epsilon = 4t$, $\boldsymbol{b} = (0,0,0)$ for TI.

time-reversal-symmetry-breaking perturbations b_x, as shown in Fig. 6(a). In Fig. 6(b) ϵ/t parametrizes the flow from the TI to the WSM, which shows a switching from inter- to intraorbital pairing as one moves from the TI to the WSM. We show the pairing amplitudes in Fig. 7 at $z = 0$ as a function of the coupling to the superconductor $\lambda_S = \pi N(0)(\tilde{t})^2$ and as a function of the the superconducting pairing amplitude Δ and in general, we see that all the pairing amplitudes increase as the parameters increase.

V. SURFACE STATES AND COMPARISON WITH EXACT DIAGONALIZATION

Finally, we discuss the effect of superconducting proximity on the surface states and we compare the results from the Green's function method with an exact diagonalization. After computing the self-energy of the electrons in the WSM due to the proximity effect as in Eq. (8), we can construct the effective band structure by solving

$$\mathrm{Det}\,[H_{\mathrm{W}} + \Sigma(\omega) - \omega] = 0, \tag{16}$$

which, in turn, is the equivalent of finding the peaks in the LDOS of the system. For the case of the TI, the surface state acquires an induced pairing which gaps the surface band completely in agreement with earlier results [16], whereas for the surface state of the WSM, the induced gap is much smaller and actually vanishes at the Weyl nodes. This is shown in Figs. 8(a) and 8(b), where the effective band structure of the WSM in proximity with a superconductor is plotted as a function of k_x and k_y, respectively. The same band structure has also been plotted using exact diagonalization. Note that Fig. 8 is only the band structure at the surface in proximity to the superconductor. This is why the other surface state, with opposite chirality, is not visible here. The first point to note is that there is no qualitative difference in the band structure using the Green's function technique and using exact diagonalization. This clearly justifies the approximation of using only the on-site or local component in the self-energy. Also, note that in contrast to the dispersion in Fig. 2 without the proximity effect, we see here that the proximity to the superconductor has split the flat band into two, giving rise to a small anisotropic gap. However, the states at the Weyl nodes are not gapped. This is not unexpected because the s-wave superconducting correlations couples the electrons at one node of a certain chirality to holes at the other node of the *same* chirality (because the two nodes have opposite chirality, but the holes and electrons also have opposite chirality); hence, no gap can open up [24]. It is also of interest to consider the band structure as a function of k_y as shown in Fig. 8(b). The edge states of the Chern insulator for each fixed value of k_x between the nodes, are now split by the proximity effect into two edge states, each carrying *half* the Chern number of the original edge state. We also compare the LDOS computation with an exact diagonalization and as can be seen in the figure, the results match quite well.

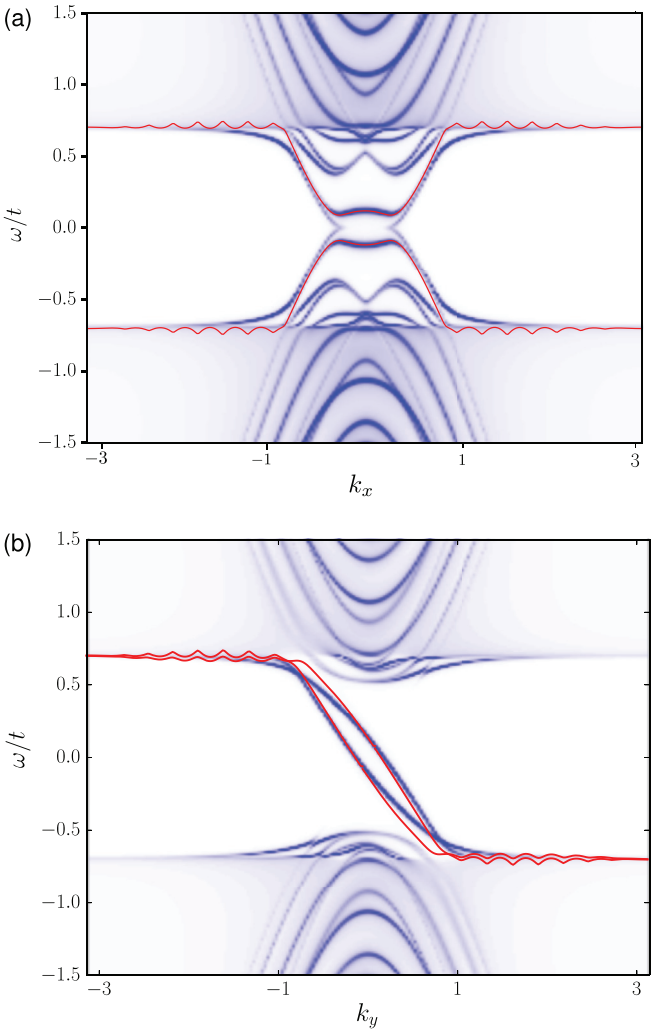

FIG. 8. (Color online) Comparison of the Green's function technique that we used with exact diagonalization results for the effect of the proximity-induced superconductivity in the surface bands of the WSM with momenta (a) k_x and (b) k_y where the Weyl nodes lie along k_x. The blue (gray) high-density lines are the modified bands in the system with proximity to the superconductor obtained from the LDOS at $z = 0$, while the red (darker) solid line is the surface band at $z = 0$ via exact diagonalization. Note that we have only depicted the surface band at $z = 0$ and have suppressed the other surface state. The induced gap vanishes at the Weyl nodes for a large enough system size, but the surface band splits. The various parameters that have been used for the LDOS are $\lambda_{\mathrm{SO}} = \lambda_z = 0.5t$, $\Delta = 0.7t$, $\lambda_S = 0.9t$, $\epsilon = 6t$, $\boldsymbol{b} = (0.5t,0,0)$ and the number of sites in z has been taken to be 20. We have used $k_y = 0$ for (a) and $k_x = 0$ for (b).

VI. DISCUSSION AND CONCLUSIONS

In summary, we have provided a detailed study of proximity-induced superconductivity in Weyl semimetals. We have focused on the proximity of the s-wave superconductor in the current work, though a similar analysis can also be made for p-wave and d-wave superconductors. We find that despite the presence of bulk metallic states in the WSM, the induced pairing remains confined to a few layers close to the interface and in fact, falls off exponentially fast away from the interface. We note that the s-wave superconductor induces both s-wave and p-wave pairing, but the induced p-wave pairing is always smaller than the dominant s-wave pairing. We also find that increasing the chemical potential does not increase either the

penetration into the bulk or the ratio between the p-wave and the s-wave amplitudes significantly. Both s-wave and p-wave components of the induced pairing can, however, be increased by increasing the pairing amplitude in the superconductor or by increasing the coupling to the superconductor.

ACKNOWLEDGMENTS

U.K., S.P., and S.R. would like to thank J. D. Sau for useful discussions. Computational work for this study was carried out at the cluster computing facility in the Harish-Chandra Research Institute (http://www.hri.res.in/cluster). A.K. was supported by the College of Arts and Science and the Offices of the Vice President for Research and the Vice Provost for Research at Indiana University. We would also like to thank the anonymous referee for comments, which were helpful in improving the clarity and presentation of the work.

APPENDIX: COMPUTATION OF THE SELF-ENERGY

We compute the self-energy of the Weyl semimetal electrons tunnel-coupled to a superconductor along one of its surfaces, following Ref. [29]. The complete Hamiltonian is given as

$$H = H_C + H_{SO} + H_E + H_S + H_T, \tag{A1}$$

where $H_C + H_{SO}$ is given in Eq. (1), H_E is given in Eq. (3), H_S is given in Eq. (4), and H_T is given in Eq. (5). We work in the Nambu basis for the fermions given in Eq. (6). In this basis the Hamiltonian for the WSM is $H_W = H_C + H_{SO} + H_E$ with

$$\begin{aligned} H_C &= -t \sum_{\langle \boldsymbol{r},\boldsymbol{r}'\rangle} \tilde{\Psi}^\dagger_{\boldsymbol{r}} h_c \tilde{\Psi}_{\boldsymbol{r}'} + \text{H.c.} + \epsilon \sum_{\boldsymbol{r}} \tilde{\Psi}^\dagger_{\boldsymbol{r}} h_c \tilde{\Psi}_{\boldsymbol{r}}, \\ H_{SO} &= \sum_{\boldsymbol{r}} \tilde{\Psi}^\dagger_{\boldsymbol{r}} h_{sx} \tilde{\Psi}_{\boldsymbol{r}+\boldsymbol{x}} + \sum_{\boldsymbol{r}} \tilde{\Psi}^\dagger_{j} h_{sy} \tilde{\Psi}_{\boldsymbol{r}+\boldsymbol{y}} \\ &\quad + \sum_{\boldsymbol{r}} \tilde{\Psi}^\dagger_{\boldsymbol{r}} h_{sz} \tilde{\Psi}_{\boldsymbol{r}+\boldsymbol{z}} + \text{H.c.}, \\ H_E &= \sum_{\boldsymbol{r}} \tilde{\Psi}^\dagger_{\boldsymbol{r}} h_E \tilde{\Psi}_{\boldsymbol{r}}. \end{aligned} \tag{A2}$$

The various h matrices defined above are given as

$$\begin{aligned} &h_c = \eta^z \tau^z \mathbf{I}_\sigma, \quad h_{sx} = \lambda_{SO} \eta^z \tau^z \sigma^y, \\ &h_{sy} = \lambda_{SO} \eta^z \tau^z \sigma^x, \quad h_{sz} = i\lambda_z \eta^z \tau^y \mathbf{I}_\sigma, \\ &h_E = (b_o \eta^z \tau^y \sigma^z) + (-b_x \mathbf{I}_\eta \tau^x \sigma^x + b_y \mathbf{I}_\eta \tau^x \sigma^y + b_z \mathbf{I}_\eta \mathbf{I}_\tau \sigma^z), \end{aligned} \tag{A3}$$

where, as mentioned below Eq. (1), $\boldsymbol{\sigma}$ and $\boldsymbol{\tau}$ denote Pauli matrices in spin and parity (orbital) space and $\boldsymbol{\eta}$ represents the particle-hole pseudospin.

For the superconductor, we only require a 4-component Nambu basis $\tilde{\Phi}^\dagger_{\boldsymbol{R}} = (\phi^\dagger_{\boldsymbol{R}\uparrow}, \phi^\dagger_{\boldsymbol{R}\downarrow}, \phi_{\boldsymbol{R}\downarrow}, -\phi_{\boldsymbol{R}\uparrow})$. In this basis, the Hamiltonian for the superconductor, Eq. (4), is

$$\begin{aligned} H_S &= \sum_{\boldsymbol{R}} \tilde{\Phi}^\dagger_{\boldsymbol{R}} (\epsilon_{\text{sc}} \eta^z + \Delta \eta^x) \mathbf{I}_\sigma \tilde{\Phi}_{\boldsymbol{R}} \\ &\quad - t_{\text{sc}} \sum_{\langle \boldsymbol{R},\boldsymbol{R}'\rangle} \tilde{\Phi}^\dagger_{\boldsymbol{R}} \eta^z \mathbf{I}_\sigma \tilde{\Phi}_{\boldsymbol{R}'} + \text{H.c.} \end{aligned} \tag{A4}$$

The coupling between the semimetal fermions and the fermions in the superconductor, Eq. (5), is

$$H_T = \sum_{\boldsymbol{r},\boldsymbol{R}} \tilde{\Psi}^\dagger_{\boldsymbol{r}} A_{\boldsymbol{r},\boldsymbol{R}} \tilde{\Phi}_{\boldsymbol{R}} + \text{H.c.}, \tag{A5}$$

where

$$A_{\boldsymbol{r},\boldsymbol{R}} = \delta_{\boldsymbol{r},\boldsymbol{r}_c} \delta_{\boldsymbol{R},\boldsymbol{r}+z} \begin{pmatrix} \tilde{t}_1 & 0 & 0 & 0 \\ 0 & \tilde{t}_1 & 0 & 0 \\ \tilde{t}_2 & 0 & 0 & 0 \\ 0 & \tilde{t}_2 & 0 & 0 \\ 0 & 0 & -\tilde{t}_1 & 0 \\ 0 & 0 & 0 & -\tilde{t}_1 \\ 0 & 0 & -\tilde{t}_2 & 0 \\ 0 & 0 & 0 & -\tilde{t}_2 \end{pmatrix}. \tag{A6}$$

The total action for the system can now be written as

$$S = \int_{-\infty}^{\infty} dt \left[\sum_{\boldsymbol{R}} \tilde{\Phi}^\dagger_{\boldsymbol{R}} [i\hbar\partial_t] \tilde{\Phi}_{\boldsymbol{R}} + \sum_{\boldsymbol{r}} \tilde{\Psi}^\dagger_{\boldsymbol{r}} [i\hbar\partial_t] \tilde{\Psi}_{\boldsymbol{r}} - H \right],$$

where H is the complete Hamiltonian given in Eq. (A1). After taking a Fourier transform over time, the action can be written in terms of the bare Green's functions of the superconductor and the WSM as follows:

$$\begin{aligned} S = \int_{-\infty}^{\infty} \frac{d\omega}{2\pi} \sum_{\boldsymbol{R},\boldsymbol{R}',\boldsymbol{r},\boldsymbol{r}'} &\big[\tilde{\Phi}^\dagger_{\boldsymbol{R}} \mathcal{G}^{-1}_{\boldsymbol{R},\boldsymbol{R}'}(\omega) \tilde{\Phi}_{\boldsymbol{R}'} + \tilde{\Psi}^\dagger_{\boldsymbol{r}} G^{-1}_{B\boldsymbol{r},\boldsymbol{r}'}(\omega) \tilde{\Psi}_{\boldsymbol{r}'} \\ &+ \tilde{\Phi}^\dagger_{\boldsymbol{R}} A^\dagger_{\boldsymbol{R},\boldsymbol{r}} \tilde{\Psi}_{\boldsymbol{r}} + \tilde{\Psi}^\dagger_{\boldsymbol{r}} A_{\boldsymbol{r},\boldsymbol{R}} \tilde{\Phi}_{\boldsymbol{R}} \big], \end{aligned} \tag{A7}$$

where $\mathcal{G}(\omega)$ and $G_B(\omega)$ are the bare Green's functions of the superconductor and the semimetal, respectively. We now define

$$\tilde{\chi}_{\boldsymbol{R}} = \tilde{\Phi}_{\boldsymbol{R}} + \sum_{\boldsymbol{r},\boldsymbol{R}'} \mathcal{G}_{\boldsymbol{R},\boldsymbol{R}'}(\omega) A^\dagger_{\boldsymbol{R}',\boldsymbol{r}} \tilde{\Psi}_{\boldsymbol{r}}$$

and obtain

$$S = \int_{-\infty}^{\infty} \frac{d\omega}{2\pi} \left[\sum_{\boldsymbol{R},\boldsymbol{R}'} \tilde{\chi}^\dagger_{\boldsymbol{R}} \mathcal{G}^{-1}_{\boldsymbol{R},\boldsymbol{R}'}(\omega) \tilde{\chi}_{\boldsymbol{R}'} + \sum_{\boldsymbol{r},\boldsymbol{r}'} \tilde{\Psi}^\dagger_{\boldsymbol{r}} G^{-1}_{\boldsymbol{r},\boldsymbol{r}'}(\omega) \tilde{\Psi}_{\boldsymbol{r}'} \right],$$

where $G^{-1}(\omega) = G_B^{-1}(\omega) - \Sigma(\omega)$ is the inverse of the full Green's function and the self-energy is given by

$$\Sigma_{\boldsymbol{r},\boldsymbol{r}'}(\omega) = \sum_{\boldsymbol{R},\boldsymbol{R}'} A_{\boldsymbol{r},\boldsymbol{R}} \mathcal{G}_{\boldsymbol{R},\boldsymbol{R}'}(\omega) A^\dagger_{\boldsymbol{R}',\boldsymbol{r}'}. \tag{A8}$$

The two fields $\tilde{\chi}$ and $\tilde{\Psi}$ are decoupled and the effect of the superconductor on the WSM is encoded in the self-energy term. Now, we approximate $\mathcal{G}$ by the bulk Green's function of the superconductor given by

$$\begin{aligned} \mathcal{G}_{\boldsymbol{R},\boldsymbol{R}'}(\omega) = \sum_{\boldsymbol{K}} &\frac{e^{i\boldsymbol{K}\cdot(\boldsymbol{R}-\boldsymbol{R}')}}{\omega^2 - (\xi_K^2 + \Delta^2)} \\ &\times \begin{pmatrix} \omega + \xi_K & 0 & \Delta & 0 \\ 0 & \omega + \xi_K & 0 & \Delta \\ \Delta & 0 & \omega - \xi_K & 0 \\ 0 & \Delta & 0 & \omega - \xi_K \end{pmatrix}, \end{aligned}$$

where $\boldsymbol{K}$ is the momentum in all three dimensions and $\xi_K = \epsilon_{\text{sc}} - 2t_{\text{sc}} \sum_i \cos K_i$. This approximation essentially ignores any surface effects that might exist in the superconductor itself. We ignore these, since the surface effects of a superconductor are not of primary interest here.

Then assuming $\tilde{t}$ to be the same for both the orbitals, the on-site ($\boldsymbol{r} = \boldsymbol{r}'$) self-energy is

$$\Sigma_{\boldsymbol{r},\boldsymbol{r}}(\omega) = (\tilde{t})^2 \delta_{\boldsymbol{r},\boldsymbol{r}_c} \sum_{\boldsymbol{K}} \frac{1}{\omega^2 - \left(\xi_{\boldsymbol{K}}^2 + \Delta^2\right)} \times [\omega \mathbf{I}_\eta - \Delta \eta^x + \xi_{\boldsymbol{K}} \eta^z](\mathbf{I}_\tau + \tau^x)\mathbf{I}_\sigma . \quad \text{(A9)}$$

Summing over the momenta, we get the final expression for self-energy to be

$$\Sigma_{\boldsymbol{r}}(\omega) = \delta_{\boldsymbol{r},\boldsymbol{r}_c} \frac{\pi N(0)(\tilde{t})^2}{\sqrt{\Delta^2 - \omega^2}} [\omega \mathbf{I}_\eta - \Delta \eta^x](\mathbf{I}_\tau + \tau^x)\mathbf{I}_\sigma , \quad \text{(A10)}$$

as used in the main text.

[1] M. Buttiker, Science **325**, 278 (2009); M. Z. Hasan and C. L. Kane, Rev. Mod. Phys. **82**, 3045 (2010); X.-L. Qi and S.-C. Zhang, *ibid.* **83**, 1057 (2011).

[2] K. von Klitzing, G. Dorda, and M. Pepper, Phys. Rev. Lett. **45**, 494 (1980); D. C. Tsui, H. L. Stormer, and A. C. Gossard, *ibid.* **48**, 1559 (1982); R. E. Prange and S. M. Girvin, *The Quantum Hall Effect* (Springer-Verlag, New York, 1990).

[3] C. L. Kane and E. J. Mele, Phys. Rev. Lett. **95**, 226801 (2005); **95**, 146802 (2005); C. Wu, B. A. Bernevig, and S. C. Zhang, *ibid.* **96**, 106401 (2006); B. A. Bernevig, T. L. Hughes, and S. C. Zhang, Science **314**, 1757 (2006); J. E. Moore and L. Balents, Phys. Rev. B **75**, 121306 (2007); R. Roy, *ibid.* **79**, 195321 (2009); M. König, H. Buhmann, L. W. Molenkamp, T. L. Hughes, C.-X. Liu, X. L. Qi, and S. C. Zhang, J. Phys. Soc. Jpn. **77**, 031007 (2008); M. König, S. Wiedmann, C. Brune, A. Roth, H. Buhmann, L. Molenkamp, X.-L. Qi, and S.-C. Zhang, Science **318**, 766 (2007).

[4] A. P. Schnyder, S. Ryu, A. Furusaki, and A. W. W. Ludwig, Phys. Rev. B **78**, 195125 (2008).

[5] L. Fidkowski and A. Kitaev, Phys. Rev. B **81**, 134509 (2010).

[6] X. Wan, A. M. Turner, A. Vishwanath, and S. Y. Savrasov, Phys. Rev. B **83**, 205101 (2011); A. A. Burkov and L. Balents, Phys. Rev. Lett. **107**, 127205 (2011); P. Hosur, S. A. Parameswaran, and A. Vishwanath, *ibid.* **108**, 046602 (2012).

[7] A. A. Burkov, M. D. Hook, and L. Balents, Phys. Rev. B **84**, 235126 (2011).

[8] P. Delplace, J. Li, and D. Carpentier, Europhys. Lett. **97**, 67004 (2012); A. A. Zyuzin, S. Wu, and A. A. Burkov, Phys. Rev. B **85**, 165110 (2012); V. Aji, *ibid.* **85**, 241101 (2012); T. Ojanen, *ibid.* **87**, 245112 (2013); Z. Huang, D. P. Arova, and A. V. Balatsky, New J. Phys. **15**, 123019 (2013).

[9] A. A. Zyuzin and A. A. Burkov, Phys. Rev. B **86**, 115133 (2012); Y. Chen, S. Wu, and A. A. Burkov, *ibid.* **88**, 125105 (2013); P. Goswami and S. Tewari, *ibid.* **88**, 245107 (2013).

[10] A. M. Turner and A. Vishwanath, arXiv:1301.0330; P. Hosur and X. Qi, C. R. Phys. **14**, 857 (2013).

[11] Y. S. Hor *et al.*, Phys. Rev. Lett. **104**, 057001 (2010).

[12] L. Fu and E. Berg, Phys. Rev. Lett. **105**, 097001 (2010).

[13] M. Sato, Phys. Rev. B **81**, 220504(R) (2010).

[14] S. Sasaki *et al.*, Phys. Rev. Lett. **107**, 217001 (2011).

[15] L. Fu and C. L. Kane, Phys. Rev. Lett. **100**, 096407 (2008).

[16] T. D. Stanescu, J. D. Sau, R. M. Lutchyn, and S. Das Sarma, Phys. Rev. B **81**, 241310(R) (2010).

[17] P. Sitthison and T. D. Stanescu, Phys. Rev. B **90**, 035313 (2014).

[18] Y. Tanaka, T. Yokoyama, and N. Nagaosa, Phys. Rev. Lett. **103**, 107002 (2009).

[19] J. Linder, Y. Tanaka, T. Yokoyama, A. Sudbo, and N. Nagaosa, Phys. Rev. Lett. **104**, 067001 (2010).

[20] A. M. Black-Schaffer and A. V. Balatsky, Phys. Rev. B **87**, 220506(R) (2013).

[21] A. M. Black-Schaffer and A. V. Balatsky, Phys. Rev. B **88**, 104514(R) (2013).

[22] Y. Tanaka, M. Sato, and N. Nagaosa, J. Phys. Soc. Jpn. **81**, 011013 (2012).

[23] T. O. Wehling, A. M. Black-Schaffer, and A. V. Balatsky, Adv. Phys. **63**, 1 (2014).

[24] T. Meng and L. Balents, Phys. Rev. B **86**, 054504 (2012).

[25] G. Y. Cho, J. H. Bardarson, Y. M. Lu, and J. E. Moore, Phys. Rev. B **86**, 214514 (2012).

[26] K. Lee, A. Vaezi, M. H. Fischer, and E. Kim, arXiv:1402.3297.

[27] M. M. Vazifeh and M. Franz, Phys. Rev. Lett. **111**, 027201 (2013).

[28] L. Fu and C. L. Kane, Phys. Rev. B **76**, 045302 (2007).

[29] D. Chevallier, P. Simon, and C. Bena, Phys. Rev. B **88**, 165401 (2013).

[30] M. Sigrist and K. Ueda, Rev. Mod. Phys. **63**, 239 (1991).

[31] We have checked that even though the WSM breaks time-reversal symmetry, the nonunitarity of the triplet pairing matrix is very small and does not give rise to any significant finite magnetic moment for the Cooper pair.